# Drying Endpoint Calculation and Criterion Bias Analysis for Medicinal Materials with Shrinkage

**Xi Yang**
School of Mathematics and Statistics,
Yancheng Teachers University
Yancheng 224002, Jiangsu, China
Email: y62026252@gmail.com
This work was supported by the College Student
Innovation and Entrepreneurship Training Program.
https://doi.org/10.56201/ijasmt.vol.12.no10.2026pg1.15

***Abstract***
*The interior of a medicinal material may remain insufficiently dried even when its surface or average moisture content meets the specified threshold. This study develops a heat and mass transfer workflow with a prescribed shrinkage trajectory and wettest-point endpoint calculation to quantify early triggering by alternative endpoint criteria. Shape-preserving piecewise cubic Hermite interpolation reconstructs the radius, and the moving domain is mapped to material coordinates. An implicit finite volume method with Picard iteration solves the state-dependent temperature and moisture fields. An event function based on the domain-wide maximum moisture content locates the first threshold crossing through bisection with repeated field solutions. Maximum, surface, and volume-average criteria are compared along the same deterministic simulation trajectory. At a dry-basis moisture threshold of 0.15 kg/kg, the numerical wettest-point endpoint is 51.1705 h. The surface and average criteria trigger approximately 38.39 h and 16.15 h earlier, respectively. At the first saved time after each alternative criterion triggers, the maximum moisture contents remain 0.6721 kg/kg and 0.1974 kg/kg. Thus, local or average compliance cannot replace domain-wide compliance in this case, and endpoint assessment should report both timing differences and internal threshold exceedance. The relationship between maximum-moisture error and the threshold-crossing slope further shows that event-bracket resolution is not equivalent to prediction accuracy. Supplementary comparisons of grids, time steps, geometry with identical material properties, and ambient-condition extrapolation preserve the criterion ordering under the tested settings. However, the absolute endpoint depends on discretization and boundary assumptions. These results are conditional on the prescribed radius trajectory and extrapolated ambient conditions; their applicability to actual stopping decisions requires independent experimental validation.*

***Keywords:*** *medicinal material drying; shrinkage; heat and mass transfer; wettest point; endpoint criterion; finite volume method*

## 1 Introduction

Determining the drying endpoint of medicinal materials requires attention to both overall water loss and residual internal moisture. In materials with appreciable radial transport resistance, the surface responds first to hot-air conditions, whereas internal moisture migrates gradually by diffusion. If acceptance requires a moisture limit to be met throughout the material, surface or average moisture may reach that limit before the last wet point does. An

endpoint model must therefore answer two questions: when the entire moisture field first satisfies the threshold, and how much earlier an available local or average indicator would trigger. Thin-layer drying models describe overall water-loss curves using relatively few parameters [1-2], whereas distributed transport models provide internal temperature and moisture fields [3-4]. Shrinkage studies additionally incorporate evolving geometry, deformation-related transport, and thermal effects of evaporation [5-9]. These studies provide a basis for endpoint analysis, but numerical field outputs must still be explicitly linked to acceptance conditions. Average drying curves, local measurement curves, and domain-wide maxima represent different state quantities. They cannot be interchanged at the same threshold without evidence of spatial uniformity. For endpoint calculation under prescribed operating conditions, this study combines the competition-provided shrinkage trajectory, state-dependent transport equations, and wettest-point event localization into a consistent numerical workflow. With the model, material properties, and boundary inputs fixed, only the endpoint criterion is changed. The triggering times of three indicators and the internal maximum moisture content at triggering are then compared. The focus is to identify decision bias caused by criterion selection and distinguish it from numerical solution errors and boundary-extrapolation errors. These comparisons provide testable metrics for subsequent independent validation.

## 2 Related work and scope of this study

### 2.1 Drying models for the average response

Thin-layer drying equations describe the overall response through the moisture ratio and are suitable for fitting drying curves and comparing process conditions [1-2]. However, the same average moisture content can correspond to different spatial distributions. A good fit to an overall curve therefore does not automatically ensure accurate prediction of the local maximum moisture content. Nor can it alone determine when a domain-wide moisture constraint is first satisfied.

### 2.2 Distributed heat and mass transfer models

Models based on heat conduction, moisture diffusion, and porous-media descriptions can reconstruct internal fields and analyze transport using state-dependent material properties [3-4]. For endpoint tasks, model evaluation must also address the specific output of interest. Errors in temperature fields, moisture fields, overall water loss, and the wettest-point compliance time are not equivalent. Here, the domain-wide maximum moisture content defines the endpoint function. Its differences from the surface and volume-average values quantify the extent to which alternative indicators overlook an insufficiently dried interior.

### 2.3 Shrinkage and moving boundaries

Shrinkage changes diffusion distances, control volumes, and surface-exchange scales. Mayor and Sereno [5] and Katekawa and Silva [6] reviewed drying models incorporating shrinkage. Hassini et al. [7] examined its influence on diffusivity estimation. Adrover et al. [8] and Brasiello et al. [9] developed moving-boundary descriptions, including a non-isothermal model accounting for the thermal effects of surface evaporation. Related studies further examined geometric deformation and shrinkage mechanisms [10-11]. The present study uses a prescribed radius series to describe geometric evolution rather than identifying a shrinkage constitutive relation. Its connection to this literature lies in converting distributed fields within a moving domain into comparable endpoint criteria.

### 2.4 Research objectives and applicability

This study has three components. First, under uniform radial shrinkage, the fixed dry mass of each material element provides the moisture-storage basis linking evolving geometry to the nonlinear finite volume solution. Second, differences in triggering time and internal threshold exceedance are quantified along the same trajectory, avoiding confounding from changes in the model. Third, event-bracket resolution, discrete-equation residuals, and physical prediction errors are distinguished, and conditions governing moisture-error propagation to endpoint-time error are examined. PCHIP, the finite volume method, Picard iteration, and bisection follow established numerical principles [12-14]. The contribution is therefore endpoint-oriented modeling, criterion comparison, and interpretation of errors.

## 3 Problem formulation

The medicinal material is approximated as an axisymmetric cylinder of length L = 25 cm and initial radius R0 = 2 cm. Axial gradients and transport through the end faces are neglected. The initial temperature is 28 °C, and the initial moisture content is 2.55 kg/kg [15]. Here, T(r,t) denotes temperature and C(r,t) denotes dry-basis moisture content, defined as water mass divided by dry-solid mass. All property functions use C in kg/kg. Percentages in figures and tables represent 100C, not wet-basis moisture content. The competition problem requires $C < 0.15$ kg/kg everywhere. This study defines the endpoint as the critical event at which the domain-wide maximum M(t) first reaches 0.15 kg/kg. Its numerical approximation is the right-end state of a bracket satisfying $M \leq 0.15$ kg/kg. Table 1 lists the three criteria and their interpretive limits.

**Table 1. Endpoint criteria and their interpretive limits**

| Criterion | Definition | Interpretive limit |
|---|---|---|
| Domain maximum | $M(t) \leq 0.15$ kg/kg | Critical event at which the domain-wide moisture constraint is first satisfied |
| Surface value | $C_{suf}(t) \leq 0.15$ kg/kg | Cannot exclude an insufficiently dried interior |
| Volume average | $\Sigma V_i C_i / \Sigma V_i \leq 0.15$ kg/kg | Cannot substitute for the domain maximum |
| Numerical endpoint | Right endpoint th of the bisection bracket | Event-localization approximation without a process safety margin |
| Comparison conditions | Same model, trajectory, and threshold | Criterion differences, not prediction errors against measurements |

Ambient inputs cover 0–4 h, whereas radius inputs cover 0–72 h. The predicted endpoint occurs after the ambient record ends. The numerical endpoint is therefore conditional on the prescribed radius trajectory and extrapolated late-stage ambient conditions. The radius series also contains information from times later than the calculation start, so the current results do not demonstrate online advance-prediction capability. Practical stopping applications require geometric information from real-time observations or a validated shrinkage model, together with explicit assumptions about future ambient predictions or control conditions.

## 4 Heat and mass transfer and endpoint events in a shrinking domain

### 4.1 Nonlinear radial transport equations

Radial transport is described by Fourier heat conduction and Fickian diffusion. Density ρ(C),

specific heat capacity cp(C), and thermal conductivity k(C) are updated with moisture content. The effective diffusivity D(T, C) is updated with temperature and moisture content. Equation (1) retains k and D inside the divergence operators, facilitating shared interfacial fluxes between adjacent control volumes [13-14]. In the shrinking domain, the time derivatives are interpreted as material derivatives. Section 4.3 relates physical coordinates to fixed material coordinates.

$$\rho(C)c_p(C)\frac{\partial T}{\partial t} = \frac{1}{r}\frac{\partial}{\partial r}\left(rk(C)\frac{\partial T}{\partial r}\right)$$
$$\frac{\partial C}{\partial t} = \frac{1}{r}\frac{\partial}{\partial r}\left(rD(T,C)\frac{\partial C}{\partial r}\right) \quad (1)$$

The initial temperature and moisture fields are uniform. Symmetry imposes zero gradients at the center, and the outer surface satisfies the Robin exchange conditions in Eq. (2). The heat transfer coefficient hT = 25 W/(m²·K) and mass transfer coefficient hM = $8\times10^{-7}$ m/s are taken from Appendix 2 of the competition problem [15] and held constant. T∞ is the ambient temperature, and C∞ is a boundary driving quantity constructed from the supplied ambient moisture series. In this case, C∞ is treated as compatible with the material dry-basis moisture content; this is a modeling convention under the problem assumptions. If the original ambient quantity is defined per unit mass of dry air, conversion requires a sorption-equilibrium or interfacial mass-transfer relation. Identical units alone do not justify equating the two quantities.

$$\frac{\partial T}{\partial r}\Big|_0 = \frac{\partial C}{\partial r}\Big|_0 = 0$$
$$k\frac{\partial T}{\partial r}\Big|_R = h_T(T_\infty - T_R), \qquad -D\frac{\partial C}{\partial r}\Big|_R = h_M(C_R - C_\infty) \quad (2)$$

Temperature and moisture fields are coupled through property updates. Latent heat of evaporation, vapor pressure, and deformation stress are not explicitly included. The functions for ρ, cp, k, and D are the empirical relations in Appendix 4 of the competition problem [15], not parameters reidentified from independent experiments in this study. The diffusivity exponent contains −0.30/C and −3850/TK, where TK is absolute temperature. The resulting temperature evolution and its effects on diffusivity are consequently constrained by these empirical properties and thermal-model simplifications.

**4.2 First threshold crossing at the wettest point**

Let M(t) denote the maximum dry-basis moisture content of the reconstructed radial field, with threshold Cthr = 0.15 kg/kg. The event function Φ(t) and first threshold-reaching time t* are defined in Eq. (3). For a continuous, decreasing trajectory that crosses the threshold, t* is the infimum of the set of times satisfying strict compliance.

$$\Phi(t) = \max_{0\le r\le R(t)} C(r,t) - C_{\text{thr}}, \qquad t^* = \inf\{t \ge 0 : \Phi(t) \le 0\} \quad (3)$$

The numerical endpoint is denoted by th. Existing calculation records give th = 51.1705295139 h, reported here as 51.1705 h. At the right bracket endpoint, the maximum moisture content is approximately $3.38\times10^{-9}$ kg/kg below the threshold. This difference is a numerical margin produced by localization, not a process safety margin. Neither the surface

value nor an average with nonnegative volume weights can exceed the domain-wide maximum. Compliance of the maximum therefore implies compliance of both alternatives, but the converse does not hold. Accordingly, the implementation must search for the maximum over the adopted reconstructed field rather than prespecifying the center as the only candidate location.

### 4.3 Material-coordinate representation of shrinkage

Shape-preserving piecewise cubic Hermite interpolation (PCHIP) reconstructs the supplied R(t), preserving shape over intervals with monotonic data [12]. Under uniform radial shrinkage, a material point satisfies r = R(t)ξ, with fixed material coordinate ξ ∈ [0,1] and radial velocity v = rR′(t)/R(t). The radius is a prescribed input rather than an inferred function of water loss or deformation stress. Equation (4) expresses heat and mass transfer in the material domain. The endpoint calculation remains within the temporal coverage of the radius data.

$$\xi = r/R(t), \qquad 0 \le \xi \le 1$$
$$\frac{\partial C}{\partial t}\Big|_{\xi} = \frac{1}{R^2 \xi}\frac{\partial}{\partial \xi}\left(\xi D \frac{\partial C}{\partial \xi}\right)$$
$$\rho c_p \frac{\partial T}{\partial t}\Big|_{\xi} = \frac{1}{R^2 \xi}\frac{\partial}{\partial \xi}\left(\xi k \frac{\partial T}{\partial \xi}\right) \tag{4}$$

The spatial derivative relation $\partial r = R^{-1}\partial\xi$ introduces $R^{-2}$ into the internal diffusion operator and $R^{-1}$ into the surface gradient. The transformed Robin conditions are given in Eq. (5). These distinct geometric factors show that shrinkage changes the scales of both internal transport and surface exchange. Endpoint changes therefore cannot be inferred solely from the proportional reduction in radius.

$$\frac{k}{R(t)}\frac{\partial T}{\partial \xi}\Big|_1 = h_T(T_\infty - T_R), \qquad -\frac{D}{R(t)}\frac{\partial C}{\partial \xi}\Big|_1 = h_M(C_R - C_\infty) \tag{5}$$

Define $\hat{C}(\xi,t) = C(R(t)\xi,t)$. The chain rule gives $\partial t\hat{C}|\xi = \partial tC|r + (R'/R)\xi\partial\xi\hat{C}$; thus, the time derivative at a fixed physical location cannot be used directly as the derivative at a fixed material location. In the current model, each material element has constant dry mass $m_{i,d}$. Its dry density is defined using the current volume $V_i(t)$ as $\rho_{d,i} = m_{i,d}/V_i(t)$, its water storage is $m_{i,d}C_i$, and the diffusive flux uses $\rho_d D\nabla C$. With uniform initial dry density and uniform radial shrinkage, $\rho_d$ is radially uniform and cancels from the moisture equation, yielding Eq. (4). The dry density $\rho_d$ used for moisture storage differs in definition from the empirical density $\rho(C)$ in the heat equation. Conservation accounting for the former cannot replace physical validation of the latter or of the heat-capacity model.

## 5 Numerical experiments and evaluation methods

### 5.1 Data sources and input processing

Inputs are taken from Problem A, Drying of Medicinal Materials, of the 2026 Contemporary Undergraduate Mathematical Contest in Modeling and its supplementary files [15]. Supplementary file 1 contains 241 ambient temperature and moisture-concentration records over 0–14400 s at 60 s intervals. Supplementary file 2 contains 145 radius records over 0–259200 s at 1800 s intervals. Ambient inputs are interpolated piecewise linearly within the recorded period. After 4 h, they are held at the means of the 7140–14400 s stable segment selected in the existing processing: 49.9677 °C and 0.0498606 kg/kg. Radius values use

PCHIP interpolation, and the moving-domain model retains the empirical properties from Appendix 4. The original manuscript Q4 case serves as the baseline. It is recomputed using the same model and extended through the numerical experiments in Section 5.6. Supplementary file 3 is only an output template and provides no independent observations of temperature or moisture fields or the endpoint.

**5.2 Implicit iteration for state-dependent transport equations**

The material coordinate is divided into N = 80 radial control volumes, with backward Euler time discretization and a main time step of $\Delta t = 1$ s. Control-volume sizes and interface areas are updated from the current cylindrical geometry. Interfacial thermal conductivities or diffusivities use the harmonic mean in Eq. (6). Adjacent interior cells share the same interfacial flux to maintain consistency of discrete exchange [13].

$$V_i = \pi L(r_{i+1/2}^2 - r_{i-1/2}^2), \qquad A_{i+1/2} = 2\pi L r_{i+1/2}$$
$$q_{i+1/2} = \frac{2q_i q_{i+1}}{q_i + q_{i+1}}, \qquad F_{i+1/2} = -A_{i+1/2} q_{i+1/2} \frac{u_{i+1} - u_i}{r_{i+1} - r_i} \tag{6}$$

At each candidate time level, Picard iteration updates ρ, cp, k, and D using the current T and C. The tridiagonal temperature and moisture systems are then solved sequentially before the properties are updated again. The existing settings use a relaxation factor of 0.85, a normalized-increment tolerance of $10^{-9}$, a discrete-equation residual tolerance of $10^{-10}$, and at most 60 iterations. A candidate time level is accepted only when both the increment and residual satisfy their tolerances. These quantities diagnose convergence of the nonlinear discrete system. Computational efficiency has not been evaluated against alternative solvers or through runtime comparisons.

**5.3 Nested field solution and event localization**

Each main time step first updates the ambient conditions and radius, solves the nonlinear fields, and evaluates the maximum-moisture event function. If adjacent converged levels satisfy $\Phi(tL) > 0$ and $\Phi(tR) \leq 0$, the original left-end state is saved and event localization begins. At each bisection trial time τ, inputs and geometric quantities are recomputed. The solver always advances from the saved left-end state by $\tau - tL$ and completes Picard iteration. The bracket is then narrowed according to the recomputed event-function sign. This procedure links event assessment to the same discrete solver rather than treating interpolation between endpoint maxima as an intermediate field solution. Once the bracket width is below 0.05 s, its right endpoint satisfying $\Phi \leq 0$ is taken as the. Sign scanning at time-step endpoints detects crossings between time levels but can miss a trajectory that crosses downward and then rises again within one step. Monotonicity checks on the saved series cannot exclude fluctuations at all unsaved times. Interpretation as the first compliance event is therefore conditional on no missed within-step crossing. Table 2 summarizes inputs, outputs, and acceptance conditions for field solution and event localization.

**Table 2. Data dependencies for field solution and event localization**

| Stage | Input and operation | Output and acceptance condition |
|---|---|---|
| Geometry and boundaries | Update R(t) and ambient inputs at the candidate time | Material-domain geometric coefficients and boundary values |
| Property update | Update ρ, cp, k, and D from current T and C | Coefficients remain positive and physically admissible |
| Field iteration | Assemble and alternately solve two tridiagonal systems | Both increments and residuals satisfy their tolerances |
| Event scan | Reconstruct the maximum from converged fields and evaluate Φ | Detect a positive-to-nonpositive crossing bracket |
| Bisection and re-solving | Advance from the saved left-end state to the trial time | Recomputed fields and event-function sign |
| Numerical acceptance | Narrow the bracket and check $\Phi \leq 0$ at the right endpoint | Bracket width below 0.05 s |

### 5.4 Comparing endpoint criteria along the same trajectory

Within a single moving-domain simulation, M(t), surface moisture content Csuf(t), and volume-average moisture content $\bar{C}V(t)$ are each compared with Cthr. The volume average is $\bar{C}V = \Sigma ViCi/\Sigma Vi$. Under the assumed radially uniform dry density, it also equals total water mass divided by total dry mass. This interpretation does not apply directly if the actual material has nonuniform dry density. The primary event is localized by bisection with repeated field solutions. Surface and average events are bracketed by the first adjacent saved records that cross the threshold in the complete series, using the one-minute output interval.

The same-trajectory comparison fixes the model, material properties, geometry, and ambient inputs. Differences among the three endpoints can therefore be attributed to the adopted criteria. This comparison addresses decision differences within the current model, not prediction errors against measured data. Evaluating shrinkage effects requires a separate fixed-radius control with identical properties. Questions 3 and 4 of the competition problem use different properties, so subtracting their endpoints cannot isolate a purely geometric effect.

### 5.5 Endpoint metrics and numerical checks

The metrics include the maximum-based numerical endpoint th, first-triggering brackets for alternative criteria, their time advances relative to th, and the maximum moisture content at triggering. Relative time advance and maximum-moisture threshold exceedance are additionally defined in Eq. (7) to characterize both timing and compliance. When an alternative event time is bracketed, its relative time advance is also reported as an interval. Threshold exceedance uses the saved value at the right bracket endpoint and is not presented as the field value at the exact triggering instant. Cumulative water and energy balance errors, nonlinear residuals, and the final event bracket check consistency of the discrete calculation; they are not experimental prediction errors.

$$\eta_{t,S} = \frac{t_h - t_S}{t_h} \times 100\%, \quad \eta_{C,S} = \frac{M(t_{R,S}) - C_{thr}}{C_{thr}} \times 100\% \quad (7)$$

Here, tS is the first triggering time of an alternative criterion, and ηt,S is its fractional time advance relative to the maximum-based endpoint. tR,S is the right endpoint of the first saved-record bracket crossing the threshold. ηC,S quantifies the relative extent to which the internal

maximum moisture content exceeds the threshold. When $\eta_{C,S} > 0$, the internal moisture constraint is still violated. Both metrics are deterministic comparisons within one simulation, not measures of experimental error or statistical significance.

### 5.6 Design of supplementary numerical experiments

To evaluate dependence on discretization, geometry treatment, and ambient extrapolation, 13 deterministic numerical runs were defined. All retain the Appendix 4 material properties, initial fields, heat and mass transfer coefficients, and 0.15 kg/kg threshold. The baseline uses $N = 80$, $\Delta t = 1$ s, the prescribed radius trajectory, and stable-segment mean extrapolation after 4 h. All runs use the same finite volume formulation, relaxation factor of 0.85, nonlinear acceptance conditions, and 0.05 s event-localization tolerance, with a common maximum duration of 72 h. Maximum, surface, and volume-average values are saved every 60 s, with an additional saved state at the maximum-based endpoint. Spatial refinement uses $N = 40$, 80, 160, and 320 at a fixed time step of 1 s. Temporal refinement uses $\Delta t = 2$, 1, and 0.5 s at $N = 80$. A joint-refinement run uses $N = 160$ and $\Delta t = 0.5$ s. Each endpoint is compared with the baseline, and successive refinement levels are checked for decreasing endpoint differences. Each discretization is solved separately. Fine-grid calculations are not treated as observations of real medicinal materials, and baseline-to-fine-grid differences are not treated as known exact errors. The geometry control replaces only the prescribed $R(t)$ with a fixed radius $R0 = 2$ cm; all other model inputs remain unchanged. Ambient controls modify only the boundary conditions after 4 h. One run holds temperature and the ambient moisture driving quantity at their last recorded values. Four additional runs perturb either the stable-segment mean temperature by ±1 °C or the mean moisture driving quantity by ±0.005 kg/kg, changing only one quantity at a time. These amplitudes define sensitivity scenarios, not sensor errors, measured environmental distributions, or statistical confidence intervals. Radius trajectories are not adjusted in response to these perturbations. The supplementary calculations reconstruct inputs from the original supplementary files rather than using existing result files as computational inputs. A program implementing the stated discretization was cross-checked against the original Python implementation over the first 600 s. Absolute differences in maximum, average, and surface moisture contents and surface temperature were all below $10^{-9}$ in their respective units of kg/kg and °C. The complete baseline recomputation was then used to check the results in Section 6.1. This checks implementation consistency, not independent physical validity, because both implementations use the same mathematical model. Complete run parameters and minute-by-minute trajectories are retained with the computational materials.

## 6 Results and analysis

### 6.1 Triggering differences between the wettest-point and alternative criteria

The domain-maximum numerical endpoint is $t_h = 51.1705$ h, at which the maximum of the reconstructed field occurs at the center. The maximum, volume-average, and surface moisture contents are approximately 0.1500, 0.1184, and 0.0525 kg/kg, respectively. The average and surface values are 0.0316 kg/kg and 0.0975 kg/kg below the maximum. Appreciable spatial moisture differences therefore remain when domain-wide compliance is achieved. Figure 1 shows the three indicators along the same trajectory.

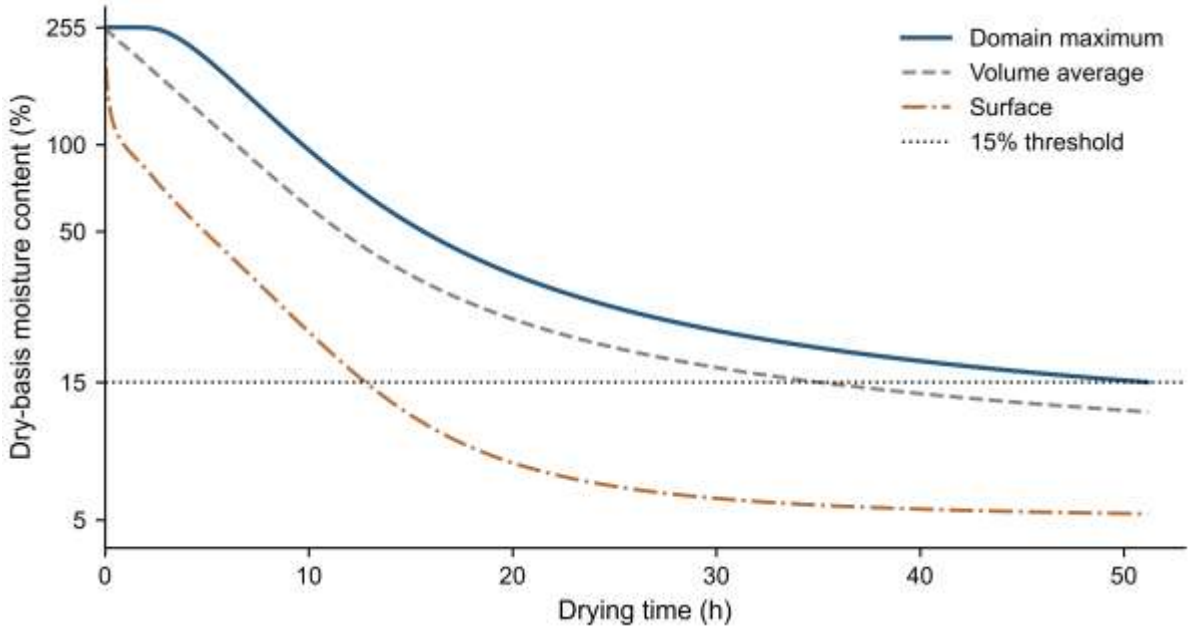



Figure 1. Maximum, volume-average, and surface dry-basis moisture contents along the same deterministic simulation trajectory. All 3072 saved records from the original calculation file analysis_q4.xlsx are used. The vertical axis is logarithmic and shows dry-basis moisture percentages; the dotted line marks the 15% threshold. The volume average is weighted by control-volume size. Saved records are time samples from one simulation trajectory, not independent experimental samples.

Surface moisture contents at 45960 s and 46020 s are 0.15026315 kg/kg and 0.14993389 kg/kg, respectively. Volume-average values at 126060 s and 126120 s are 0.15000270 kg/kg and 0.14995158 kg/kg, respectively. These values define the first-triggering brackets in Table 3. Neither an increase nor an earlier crossing was found for either indicator in the saved series. Conditional on continuous monotonic behavior between adjacent saved times, the surface criterion triggers 38.387–38.404 h before the maximum criterion, and the average criterion triggers 16.137–16.154 h earlier.

Table 3. Triggering times and internal maximum moisture contents for criteria evaluated along the same trajectory

| Criterion | First compliance time (h) | Advance relative to th (h) | Right-end maximum moisture (%) |
|---|---|---|---|
| Surface value | 12.7667–12.7833 | 38.387–38.404 | 67.21 |
| Volume average | 35.0167–35.0333 | 16.137–16.154 | 19.74 |
| Domain maximum | 51.1705 | 0 | 15.00 |

Equation (7) gives relative time advances of 75.02%–75.05% for the surface criterion and 31.54%–31.57% for the average criterion. Maximum moisture contents at the right bracket endpoints are 0.6721 kg/kg and 0.1974 kg/kg, corresponding to threshold exceedances of approximately 348.1% and 31.6%. Thus, the surface criterion has already triggered while the internal maximum is approximately 4.48 times the threshold. After the average criterion triggers, the internal maximum remains approximately 1.32 times the threshold. Relative time advance measures the timing difference, whereas threshold exceedance measures the degree of internal underdrying at early triggering.

### 6.2 Discrete consistency and event resolution

The existing calculation records report endpoint cumulative relative balance errors of $1.54\times10^{-6}$ for water and $4.85\times10^{-7}$ for energy. The maximum nonlinear-equation residual among saved records is $9.99\times10^{-11}$. Water imbalance is normalized by the initial water mass. Energy imbalance is normalized by the larger of the absolute cumulative heat transfer and 1 J. The final event-bracket width is 0.03125 s, satisfying the 0.05 s localization setting. These quantities check discrete accounting, nonlinear solution, and event localization, respectively. They do not estimate spatial or temporal discretization errors or account for uncertainty in empirical properties and ambient extrapolation.

### 6.3 Geometric scales associated with the shrinkage trajectory

At the numerical endpoint, the prescribed trajectory gives $R \approx 1.20$ cm, compared with the initial radius of 2.00 cm. The relative geometric factor for internal diffusion is $(R0/R)^2 \approx 2.78$, whereas that for the surface gradient is $R0/R \approx 1.67$. Internal transport and boundary exchange therefore undergo different changes in geometric scale. Because effective diffusivity evolves simultaneously with temperature and moisture, neither 2.78 nor 1.67 can be interpreted as a multiplicative increase in drying rate.

An existing fixed-radius case has an endpoint of 57.7056 h, but it uses the Appendix 3 material properties, whereas the moving-domain model uses Appendix 4. Geometry and material properties therefore change simultaneously, preventing interpretation of their endpoint difference as a shrinkage-only effect. A purely geometric control must retain the Appendix 4 properties, initial fields, ambient inputs, boundary coefficients, and numerical settings, comparing only R(t) with constant R0. Section 6.5 supplies this control. The original 57.7056 h result is not used to estimate the purely geometric effect.

### 6.4 Grid and time-step sensitivity

The recomputed baseline endpoint is 51.1705295 h, consistent with the retained value of 51.1705 h in Section 6.1. The first saved-record triggering brackets are also reproduced as 45960–46020 s for the surface criterion and 126060–126120 s for the average criterion. Table 4 presents the grid and time-step comparisons. The original results for the three criteria continue to be reported as the baseline.

**Table 4. Effects of discretization on the maximum-moisture endpoint**

| Run | N | Δt (s) | Numerical endpoint (h) | Difference from baseline (s) |
|---|---|---|---|---|
| Spatial refinement | 40 | 1 | 51.231814 | +220.625 |
| Baseline | 80 | 1 | 51.170530 | +0.000 |
| Spatial refinement | 160 | 1 | 51.147318 | -83.562 |
| Spatial refinement | 320 | 1 | 51.139731 | -110.875 |
| Time-step control | 80 | 2 | 51.171042 | +1.844 |
| Temporal refinement | 80 | 0.5 | 51.170295 | -0.844 |
| Joint refinement | 160 | 0.5 | 51.147083 | -84.406 |

At $\Delta t = 1$ s, increasing N from 40 to 80, 160, and 320 progressively reduces the endpoint. Successive endpoint differences are 220.63, 83.56, and 27.31 s, decreasing with refinement. The baseline and N = 320 endpoints differ by 110.87 s, approximately 0.060% of the baseline

endpoint. At fixed N = 80, reducing the time step from 1 s to 0.5 s changes the endpoint by 0.844 s. The joint-refinement endpoint is 51.147083 h. Over the tested settings, spatial refinement causes larger endpoint changes than halving the time step.

These results support a numerical refinement trend but do not establish that spatial error has vanished or that the solution has entered a confirmed asymptotic convergence regime. The surface, average, and maximum criteria retain their ordering in all Table 4 runs. Their timing differences of approximately 38 h and 16 h greatly exceed the observed endpoint differences between discretizations. Criterion ordering is therefore stable over the tested discretization settings. The 0.03125 s event-bracket width remains much smaller than the changes caused by grid refinement and cannot be interpreted as overall endpoint accuracy.

### 6.5 Fixed-radius control with identical material properties

Using the same Appendix 4 properties gives the fixed-radius control a different interpretation from the original 57.7056 h case based on Appendix 3. Only the geometric input changes in Table 5, isolating the difference attributable to the prescribed shrinkage geometry within the current model.

Table 5. Geometry comparison using Appendix 4 material properties

| Geometry | Maximum-based endpoint (h) | Simulation stop time (h) | Maximum moisture at stop (kg/kg) |
|---|---|---|---|
| Prescribed shrinkage | 51.1705 | 51.1705 | 0.150000 |
| Fixed radius of 2 cm | >72 | 72.0000 | 0.224970 |

At 72 h, the fixed-radius run still has a maximum moisture content of 0.2250 kg/kg and a volume average of 0.1676 kg/kg. It therefore does not satisfy the domain-wide threshold within the common simulation horizon. Its endpoint is at least approximately 20.83 h later than that of the prescribed-shrinkage run. The entry “>72” indicates noncompliance within the simulated period, not a computed endpoint replaced by 72 h. The result supports an influence of geometry treatment on endpoint calculation in this case. However, it remains conditional on the supplied shrinkage trajectory and model properties and cannot be directly extrapolated to an experimental shrinkage effect in real medicinal materials.

### 6.6 Sensitivity to extrapolated late-stage ambient conditions

Because the predicted endpoint occurs after the ambient record ends, the influence of boundary assumptions after 4 h must be examined separately. Inputs within the recorded period and the full radius trajectory are held unchanged while the late-stage conditions in Table 6 are imposed. The last-value-hold run uses the recorded values of 50.165 °C and 0.04986 kg/kg. All other perturbations are relative to the stable-segment means.

Table 6. Effects of late-stage ambient scenarios on the numerical endpoint

| Boundary setting after 4 h | Numerical endpoint (h) | Difference from baseline (h) | Relative change (%) |
|---|---|---|---|
| Stable-segment means | 51.1705 | +0.0000 | +0.000 |
| Last recorded values held | 50.8549 | -0.3156 | -0.617 |
| Late-stage temperature −1 °C | 52.8127 | +1.6422 | +3.209 |
| Late-stage temperature +1 °C | 49.5993 | -1.5712 | -3.071 |

| Boundary setting after 4 h | Numerical endpoint (h) | Difference from baseline (h) | Relative change (%) |
|---|---|---|---|
| Late-stage moisture −0.005 | 51.0941 | -0.0764 | -0.149 |
| Late-stage moisture +0.005 | 51.2833 | +0.1128 | +0.220 |

Note: perturbations to the late-stage moisture driving quantity are in kg/kg and retain the physical interpretation specified in Section 4.1. Positive time differences indicate later compliance than the baseline; negative differences indicate earlier compliance.

The last-value-hold endpoint is 50.8549 h, 18.94 min earlier than the baseline. Decreasing and increasing the late-stage temperature by 1 °C delays the endpoint by 1.6422 h and advances it by 1.5712 h, respectively. Decreasing and increasing the late-stage moisture driving quantity by 0.005 kg/kg advances the endpoint by 4.59 min and delays it by 6.77 min, respectively. Temperature scenarios produce larger changes for the selected perturbation amplitudes. Because the two types of perturbation have different scales, this comparison does not establish a universal cross-parameter sensitivity ranking.

Saved records in every ambient scenario still show the surface criterion triggering before the average criterion, followed by the maximum criterion. However, the absolute endpoint varies with the boundary scenario. Two conclusions must therefore be distinguished: early triggering by alternative criteria along the same trajectory persists in the tested scenarios, whereas 51.1705 h is conditional on the specified late-stage environment. These calculations neither assign probabilities to the environmental changes nor account for their feedback on shrinkage. They cannot serve as confidence intervals for actual drying time or as process guarantees.

## 7 Discussion

### 7.1 Implications of endpoint criteria for stopping decisions

In this case, early triggering by alternative criteria coincides with an internal maximum above the threshold. Reporting compliance at a measurement point or in an average alone therefore omits a state directly relevant to domain-wide acceptance. Let $S(t)$ be the surface or average indicator and define the spatial difference $gS(t) = M(t) - S(t)$. At the instant $S(t)$ reaches the threshold, $gS(t)$ is exactly the maximum-moisture exceedance above that threshold. If a reliable upper bound $bS(t)$ on $gS(t)$ can be obtained independently in engineering applications, $S(t) + bS(t) \le C_{thr}$ is sufficient for domain-wide compliance. Without such a bound, this case cannot establish universal surface or average stopping thresholds across materials or operating conditions.

### 7.2 Propagation of moisture-content errors to endpoint-time errors

Endpoint time depends on both moisture-field error and the downward slope of the maximum curve near the threshold. Equation (8) gives an error bound for the maximum operator. If the maximum absolute difference between an approximate field and a reference field on the same spatial domain is at most $\varepsilon_C$, their maxima also differ by at most $\varepsilon_C$. The reference may be a finer-discretization solution of the same model or a field constrained by independent observations. These references correspond to numerical error and prediction error including model error, respectively, and must not be conflated.

$$|\widetilde{M}(t) - M(t)| \le \|\widetilde{C}(\cdot,t) - C(\cdot,t)\|_\infty \le \varepsilon_C \quad (8)$$

If the reference maximum curve is continuously differentiable and strictly decreasing in a neighborhood containing both critical times, with a downward rate of at least $s_{min} > 0$, the mean value theorem gives Eq. (9). Here, $\tilde{t}^*$ is the exact critical time of the approximate

maximum curve, and t* is that of the reference curve. Both curves must undergo the first threshold crossing under consideration within this neighborhood.

$$|\tilde{t}^* - t^*| \leq \frac{\varepsilon_C}{s_{min}}, \quad -\frac{dM}{dt} \geq s_{min} > 0 \quad (9)$$

A flatter curve near the threshold converts a given moisture error into a larger timing difference. The 0.03125 s event bracket therefore describes only the localization scale along the computed trajectory. Relating this scale to overall timing error additionally requires estimates of εC and smin, and of the consistency of event re-solving with a common discrete trajectory. These estimates are not provided here. Equations (8) and (9) give conditional relationships for error assessment, not numerical confidence intervals for the current prediction.

### 7.3 Relationship to existing models and applicability

Compared with models describing water loss through overall curves [1-2], this study explicitly examines the maximum constraint within a distributed field. Compared with moving-boundary models incorporating shrinkage transport and surface evaporation heat [8-9], it uses a prescribed radius and simplified heat and mass transfer to focus on endpoint-criterion comparison. These choices simplify geometric calculation but make the endpoint dependent on external geometric inputs and empirical parameters. Mean extrapolation of late-stage ambient conditions directly affects long-term transport driving forces. Omitted latent heat and interfacial-equilibrium relations affect the temperature field and the physical interpretation of the moisture boundary condition. The results should therefore be treated as endpoint analysis under specified conditions. Small numerical balance errors alone do not establish applicability to actual materials.

### 7.4 Validation requirements and conditions for engineering application

The supplementary calculations in Sections 6.4–6.6 quantify the effects of discretization, geometry treatment with identical properties, and late-stage ambient assumptions. Criterion ordering remains unchanged across the tested grids, time steps, and boundary scenarios. Nevertheless, grid refinement still changes the endpoint, and late-stage scenarios produce discernible timing shifts. The numerical experiments support comparisons within the specified model, not demonstrated predictive capability for actual medicinal materials or untested conditions. Further work requires tests coupling shrinkage and environmental changes, together with physical validation using independent batches.

Physical validation requires observations independent of parameter setting and model selection. Complete ambient and geometric histories should be recorded simultaneously. Internal and surface moisture contents should be measured using the same dry-basis definition as the model to test maximum-moisture evolution and the actual endpoint. If the final objective is a quality-compliant stopping decision, the relationship between the moisture threshold and relevant medicinal-material quality indicators must also be established. The current single operating condition supports only conditional analysis under a moisture constraint, not universal performance or quality guarantees across species and dimensions.

## 8 Conclusions

This study develops a drying-endpoint calculation workflow for medicinal materials with a prescribed shrinkage trajectory. Material coordinates, a state-dependent finite volume solution, and maximum-moisture event localization link distributed fields to domain-wide acceptance conditions. Comparisons along the same trajectory identify the timing differences and internal threshold exceedances associated with criterion selection.

Under the specified conditions, the maximum-based numerical endpoint is 51.1705 h. Surface

and volume-average criteria trigger approximately 38.39 h and 16.15 h earlier, respectively. At the first saved times after these triggers, internal maximum moisture contents remain 0.6721 kg/kg and 0.1974 kg/kg. Local or average compliance therefore precedes domain-wide compliance in this case. Endpoint assessment should report both triggering time and the maximum-moisture state.

Numerical residuals, conservation checks, and event brackets characterize different parts of the discrete solution and cannot replace endpoint-accuracy validation. In the supplementary experiments, the baseline and N = 320 endpoints differ by approximately 1.85 min. The fixed-radius run with identical properties does not reach the threshold within 72 h. Changing the late-stage temperature by ±1 °C shifts the endpoint by approximately 1.6 h. These results support stable criterion ordering under the tested conditions and quantify dependence of the absolute endpoint on discretization and extrapolation assumptions. Engineering application still requires independent measurements of internal moisture, shrinkage, and the actual endpoint.

IJASMT

**References**

[1] Erbay Z, Icier F. A review of thin layer drying of foods: Theory, modeling, and experimental results [J]. Critical Reviews in Food Science and Nutrition, 2010, 50(5): 441-464. DOI: 10.1080/10408390802437063.

[2] Ratti C. Hot air and freeze-drying of high-value foods: A review [J]. Journal of Food Engineering, 2001, 49(4): 311-319. DOI: 10.1016/S0260-8774(00)00228-4.

[3] Curcio S, Aversa M, Calabrò V, et al. Simulation of food drying: FEM analysis and experimental validation [J]. Journal of Food Engineering, 2008, 87(4): 541-553. DOI: 10.1016/j.jfoodeng.2008.01.016.

[4] Kumar C, Joardder M U H, Farrell T W, et al. A porous media transport model for apple drying [J]. Biosystems Engineering, 2018, 176: 12-25. DOI: 10.1016/j.biosystemseng.2018.06.021.

[5] Mayor L, Sereno A M. Modelling shrinkage during convective drying of food materials: A review [J]. Journal of Food Engineering, 2004, 61(3): 373-386. DOI: 10.1016/S0260-8774(03)00144-4.

[6] Katekawa M E, Silva M A. A review of drying models including shrinkage effects [J]. Drying Technology, 2006, 24(1): 5-20. DOI: 10.1080/07373930500538519.

[7] Hassini L, Azzouz S, Peczalski R, et al. Estimation of potato moisture diffusivity from convective drying kinetics with correction for shrinkage [J]. Journal of Food Engineering, 2007, 79(1): 47-56. DOI: 10.1016/j.jfoodeng.2006.01.025.

[8] Adrover A, Brasiello A, Ponso G. A moving boundary model for food isothermal drying and shrinkage: General setting [J]. Journal of Food Engineering, 2019, 244: 178-191. DOI: 10.1016/j.jfoodeng.2018.09.018.

[9] Brasiello A, Venditti C, Adrover A. Non-isothermal moving boundary model for food drying [J]. Chemical Engineering Transactions, 2021, 87: 193-198. DOI: 10.3303/CET2187033.

[10] Sinha A, Bhargav A. A simplified two-dimensional model to study the effect of shrinkage during convective drying of food samples [J]. Journal of Food Engineering, 2022, 317: 110732. DOI: 10.1016/j.jfoodeng.2021.110732.

[11] Tuly S S, Putranto A, Chen X D. A mechanistic shrinkage model for food drying [J]. Journal of Food Engineering, 2025, 389: 112346. DOI: 10.1016/j.jfoodeng.2024.112346.

[12] Fritsch F N, Carlson R E. Monotone piecewise cubic interpolation [J]. SIAM Journal on Numerical Analysis, 1980, 17(2): 238-246.

[13] Patankar S V. Numerical Heat Transfer and Fluid Flow [M]. New York, NY: Hemisphere, 1980.

[14] Crank J. The Mathematics of Diffusion [M]. 2nd ed. Oxford: Clarendon Press, 1975.

[15] 2026 National College Students Mathematical Modeling Contest. Problem A: Drying of Medicinal Materials [Z]. 2026: 1-4, Appendices 1-4 and supplementary files 1-3 [in Chinese].